Journal of Positive Sciences (JPS) eISSN: 2582-9351, https://positive-sciences.com JPS. 2025 July; 5(4): 14-29

Article info
Received on: 02.06.2025
Accepted on: 28.07.2025
Published on: 31.07.2025
doi: https://doi.org/10.52688/ASP92610

Research article

Comprehensive structural, optical, and biological study of sol–gel-derived $Mg_{0.91}Fe_{0.9}O$ nanoparticles

Saba N. Saeed [1, *], Habiba Kadhim Aity [2, *], Zahraa A. Jabur [3], Areej Adnan Hateef [4], Mohammed RASHEED [5]

[1, 2, 3, 4] Scientific Research Commission, Baghdad, Iraq
[5] Production Engineering & Metallurgy College, University of Technology- Iraq, Baghdad 10066, Iraq

[*] sabaalkhafaji12@gmail.com

ABSTRACT

Non-stoichiometric magnesium–iron oxides are promising multifunctional nanomaterials, yet integrated links between structure, optics, and antimicrobial response remain insufficiently resolved. Here, $Mg_{0.91}Fe_{0.9}O$ nanoparticles were synthesized by a sol–gel route (drying at 100 °C, calcination at 550 °C) and systematically characterized by XRD, FTIR, and UV–Vis, then evaluated biologically against *Staphylococcus aureus* using the agar diffusion method (ADM) and spread plate method (SPM). FTIR revealed a spinel-type ferrite lattice with characteristic metal–oxygen stretching at ~546 cm^{-1} (tetrahedral) and ~419 cm^{-1} (octahedral), alongside surface O–H/H_2O bands at ~3439 and ~1630 cm^{-1} and a weak carbonate feature near 1468 cm^{-1}, consistent with nanostructured oxides stored in air. The UV–Vis spectrum displayed a sharp ultraviolet edge and a weak sub-gap tail. Tauc analysis of $(\alpha h\nu)^2$ versus hν (direct-allowed transition) yielded an optical band gap E_g=3.85 eV, indicating an electronically wide-gap oxide in which visible-light activity is expected to be dominated by defect/surface states rather than bulk interband absorption. Antibacterial testing against *S. aureus* showed a clear inhibition halo in ADM with diameter D=16 mm (ring width ≈ 5 mm; net inhibitory area A_{net}≈172.8 mm^2 for a 6-mm disc), indicating moderate potency at the tested loading. Complementary SPM quantified surviving cells at 275 colony-forming units (CFU), within the 30–300 countable range (Poisson relative standard error ≈ 6%), confirming a finite but reduced viable fraction after exposure. Collectively, the results connect phase-consistent structure and a wide optical gap to reproducible anti-staphylococcal activity, plausibly mediated by reactive oxygen species and limited ion release. Future work should include matched controls for log-reduction metrics, increased replication, dispersion standardization, and contact/light-assisted assays to resolve defect-driven pathways.

Keywords: $Mg_{0.91}Fe_{0.9}O$ NPs, FTIR, UV (A, E_g), *S. aureus*

INTRODUCTION

Magnesium ferrites and their derivatives have emerged as a versatile class of materials due to their exceptional structural stability, tunable magnetic properties, and promising optical and biological functionalities [1]. The Mg–Fe–O system, particularly in non-stoichiometric forms such as $Mg_{0.91}Fe_{0.9}O$, offers enhanced control over lattice defects, cation distribution, and particle morphology, which directly influence their physicochemical behavior [2]. In their ideal crystalline state, magnesium ferrites adopt an inverse spinel structure, where Mg^{2+} and Fe^{3+} ions occupy both tetrahedral (A) and octahedral (B) sites in the oxygen framework [3]. By intentionally deviating from stoichiometry, it is possible to tailor key parameters such as lattice constant, crystallite size, and electronic band structure [4], which has direct implications for optical absorption, conductivity, and catalytic activity [5].

The sol–gel method has gained prominence as a reliable, cost-effective, and scalable synthesis route for nanostructured ferrites [6]. This wet-chemical approach involves hydrolysis and polycondensation of metal precursors, forming a colloidal gel that is subsequently dried and calcined to obtain crystalline nanoparticles [7]. The sol–gel technique offers several advantages over traditional solid-state synthesis, including lower calcination temperatures, uniform cation mixing at the molecular scale, and better control of particle size distribution [8]. For $Mg_{0.91}Fe_{0.9}O$, such precise compositional control ensures consistent phase purity and enhances functional performance [9].

Optical properties play a critical role in determining the functional applications of ferrite nanoparticles. The absorption coefficient and optical band gap (E_9) can be tuned by manipulating particle size, morphology, and defect density [10]. In Mg–Fe–O systems, the band gap typically lies in the range of 1.8–2.5 eV, making them suitable for photocatalysis, solar energy harvesting, and

*Corresponding author
Mohammed RASHEED,
Applied Sciences Department, University of Technology, Baghdad, Iraq
e-mail: rasheed.mohammed40@yshoo.com

bioactive applications [11]. Band gap engineering also has significant implications for antibacterial performance, as it influences light-induced ROS generation and electron transfer processes [12].

Antibacterial activity in ferrites is attributed to multiple mechanisms: (i) dissolution of metal ions (Mg^{2+}, Fe^{3+}) that interfere with bacterial metabolic pathways, (ii) generation of reactive oxygen species leading to oxidative stress, and (iii) direct physical disruption of bacterial membranes via nanoparticle adhesion [13]. The structural differences between Gram-positive bacteria (e.g., Staphylococcus aureus) and Gram-negative bacteria (e.g., Escherichia coli) affect their susceptibility to nanoparticles [14]. Gram-positive bacteria have thicker peptidoglycan layers, whereas Gram-negative bacteria possess an additional outer membrane that can either hinder or facilitate nanoparticle penetration depending on surface charge and hydrophobicity [15].

With the increasing prevalence of antibiotic-resistant strains, there is a growing demand for multifunctional materials that combine robust structural stability, tunable optical properties, and potent antibacterial activity [16]. Non-stoichiometric $Mg_{0.91}Fe_{0.9}O$ synthesized via sol–gel offers a promising pathway to meet these requirements by enabling precise control over crystallinity, defect density, and surface chemistry. This makes it an ideal candidate for integrated structural, optical, and biological studies aimed at biomedical, environmental, and photocatalytic applications [17].

Research on magnesium ferrites and their non-stoichiometric derivatives has grown significantly over the past decade, particularly in the context of structural, optical, and antibacterial applications. Numerous studies have reported the successful synthesis of Mg–Fe–O nanoparticles using the sol–gel route, revealing the method's potential for producing fine-grained, phase-pure nanocrystals with controlled morphology [18]. For instance, Patel et al. synthesized $MgFe_2O_4$ nanoparticles via sol–gel and observed that decreasing the calcination temperature led to reduced crystallite sizes and enhanced surface area, which directly improved photocatalytic performance [19]. Similarly, Kim et al. employed a citric acid-assisted sol–gel route to achieve homogeneous cation distribution, leading to improved magnetic and dielectric properties [20].

X-ray diffraction (XRD) remains the gold standard for phase identification and crystallite size estimation in ferrite systems [21]. Studies on Mg–Fe–O have consistently shown that the inverse spinel phase can be stabilized at relatively low calcination temperatures when synthesized via sol–gel [22]. Rietveld refinement of XRD data has been widely used to determine lattice constants, cation occupancy, and microstrain, offering insights into how compositional deviations influence structural stability [23].

Fourier-transform infrared spectroscopy (FTIR) provides complementary information by identifying the characteristic metal–oxygen vibrations in tetrahedral and octahedral sites [24]. Several works have confirmed that Mg–O stretching typically appears in the higher frequency range (~600 cm^{-1}), while Fe–O vibrations dominate the lower frequency range (~400 cm^{-1}) [25]. These features shift depending on particle size, cation substitution, and defect concentrations, making FTIR a useful probe for confirming compositional tuning.

Optical studies on ferrite nanoparticles often focus on the absorption spectra and Tauc plot analysis to determine the band gap energy (E_g) [26]. The reported values for $MgFe_2O_4$ range from 1.8 eV to 2.5 eV, with smaller particles generally exhibiting higher E_g due to quantum confinement effects. For biomedical applications, tuning the band gap to optimize light-induced ROS generation has been proposed as an effective strategy for enhancing antibacterial action [27].

Antibacterial investigations have shown that ferrite nanoparticles can inhibit the growth of both Gram-positive and Gram-negative bacteria, although the efficiency varies with particle size, surface chemistry, and bacterial strain [28]. Singh et al. reported that $MgFe_2O_4$ nanoparticles demonstrated a zone of inhibition against *E. coli* and *S. aureus*, with enhanced activity observed for smaller crystallite sizes and higher defect densities [29]. Furthermore, the antibacterial mechanism has been linked to oxidative stress, membrane disruption, and ionic toxicity, with ROS generation playing a central role [30].

Despite these advancements, most studies focus on either structural/optical properties or antibacterial activity in isolation, rather than integrating these aspects into a comprehensive analysis. Few works have addressed the correlation between crystallite size, lattice strain, optical band gap, and antibacterial performance for non-stoichiometric Mg–Fe–O compositions. This integrated approach is necessary to establish a clear structure–property–function relationship, which is critical for designing multifunctional nanomaterials with predictable performance in biomedical and environmental applications [31].

Although magnesium ferrites and their derivatives have been extensively investigated, the majority of studies have examined their structural, optical, or biological characteristics in isolation, rather than integrating these aspects into a single, coherent analysis [28]. This separation of focus has limited the ability to establish robust correlations between fundamental material properties (e.g., crystallite size, lattice strain, band gap energy) and functional outcomes such as antibacterial efficiency [29]. Specifically, for non-stoichiometric $Mg_{0.91}Fe_{0.9}O$, the interplay between composition, microstructure, and optical activity remains underexplored. Without a systematic understanding of these relationships, the optimization of such materials for targeted applications is hindered [30].

From a synthesis perspective, while the sol–gel method has been recognized for producing fine-grained ferrite nanoparticles with high homogeneity, its process parameters—such as precursor ratios, pH control, gelation time, and calcination temperature—can significantly influence phase formation, defect states, and cation distribution [31]. However, the influence of deliberate magnesium deficiency (as in $Mg_{0.91}Fe_{0.9}O$) on phase purity and lattice distortion has not been sufficiently addressed [32]. This gap

*Corresponding author
Mohammed RASHEED,
Applied Sciences Department, University of Technology, Baghdad, Iraq
e-mail: rasheed.mohammed40@yshoo.com

is critical because cation imbalance affects not only the structural integrity but also electronic transitions and charge carrier dynamics, which directly impact optical absorption and ROS generation [33].

Optical properties, particularly the absorption coefficient and optical band gap (E_9), have been measured for stoichiometric $MgFe_2O_4$ and certain doped variants [34]. Yet, there is limited data on how magnesium deficiency shifts the E_9, alters defect-related absorption features, and changes light–matter interactions in a way that could enhance or suppress antibacterial activity [35]. Furthermore, no consensus exists on whether narrowing or widening the band gap in Mg–Fe–O systems is more favorable for antibacterial applications, especially when using visible light as a trigger for photocatalytic disinfection [36].

On the biological front, studies have demonstrated that ferrite nanoparticles can effectively inhibit the growth of both Gram-positive and Gram-negative bacteria, but there is a lack of standardized protocols for comparing results across different experimental setups [37]. The Agar Diffusion Method (ADM) provides information on inhibition zones but is influenced by nanoparticle diffusion rates through agar, while the Spread Plate Method (SPM) quantifies viable bacterial colonies but may underestimate antibacterial effects if ROS generation is transient or spatially localized. Very few works have used both methods in parallel to evaluate the same nanoparticle composition, making cross-validation of antibacterial results rare [38].

In summary, while sol–gel-synthesized Mg–Fe–O ferrites are promising candidates for multifunctional applications, there is a pressing need for integrated studies that:

1. Precisely control non-stoichiometry and link it to changes in crystallinity, lattice strain, and vibrational modes.
2. Quantify optical responses (absorption spectra, E_9) under identical synthesis and characterization conditions.
3. Validate antibacterial activity using both ADM and SPM for multiple bacterial strains (*E. coli*, *S. aureus*).

Without such comprehensive datasets, the design of ferrite-based antibacterial agents remains largely empirical, hindering progress in biomedical, environmental, and photocatalytic applications.

Although significant progress has been made in the synthesis and characterization of magnesium ferrites, several critical research gaps remain. First, most reported studies have focused on stoichiometric $MgFe_2O_4$ or doped variants, with very few investigating non-stoichiometric compositions such as $Mg_{0.91}Fe_{0.9}O$ [38]. Magnesium deficiency alters cation distribution between tetrahedral and octahedral sites, modifies the oxygen sublattice, and changes defect densities—all of which can profoundly affect structural, optical, and antibacterial properties. However, these effects have not been systematically studied in a unified experimental framework [39].

Second, correlation studies linking microstructural features (e.g., crystallite size, microstrain, and lattice parameter variations from XRD) with optical properties (e.g., absorption edge shift, band gap tuning) are limited [40]. While there is evidence that particle size reduction in ferrites leads to band gap widening via quantum confinement, no comprehensive datasets exist for Mg–Fe–O systems synthesized under controlled non-stoichiometric conditions. Such relationships are essential for predicting and tuning the functional performance of nanoparticles for specific applications.

Third, the role of optical properties in antibacterial performance remains unclear [41]. For many ferrite systems, antibacterial activity is primarily attributed to ion release and ROS generation, yet the possible contribution of band gap-mediated photoactivation—especially under ambient or visible light—has been largely overlooked. Given that $Mg_{0.91}Fe_{0.9}O$ may exhibit band gaps in the visible range, investigating the interplay between optical absorption and bactericidal action is critical for developing light-assisted antimicrobial agents.

Fourth, in biological testing, there is a lack of methodological consistency. The Agar Diffusion Method (ADM) provides qualitative zone-of-inhibition data, whereas the Spread Plate Method (SPM) offers quantitative viable cell counts [42]. Very few studies have implemented both methods under identical conditions for the same material, which limits the reliability of antibacterial performance comparisons. This gap is particularly important because some antibacterial effects may not be adequately captured by a single technique—ADM can underestimate activity for non-diffusive nanoparticles, while SPM can fail to reflect transient ROS-mediated damage.

Finally, there is insufficient focus on integrated characterization pipelines that combine structural (XRD, FTIR), optical (UV–Vis absorption, Tauc plots), and antibacterial assays in one comprehensive study. Bridging these datasets is essential for establishing predictive models and structure–property–function correlations that could accelerate the rational design of multifunctional ferrites.

MOTIVATION

Addressing these gaps would not only advance fundamental understanding but also have practical significance in biomedical and environmental domains. The rising prevalence of antibiotic-resistant bacteria necessitates alternative antimicrobial strategies, and metal oxide nanoparticles with tunable optical and structural properties are prime candidates. By exploring $Mg_{0.91}Fe_{0.9}O$ through an integrated experimental approach, it becomes possible to design nanomaterials whose physical properties are intrinsically linked to their biological function, paving the way for targeted, efficient, and scalable antibacterial solutions.

*Corresponding author
Mohammed RASHEED,
Applied Sciences Department, University of Technology, Baghdad, Iraq
e-mail: rasheed.mohammed40@yshoo.com

The primary objective of this study is to conduct a comprehensive structural, optical, and biological investigation of sol–gel-derived $Mg_{0.91}Fe_{0.9}O$ nanoparticles, with the goal of establishing clear correlations between synthesis parameters, microstructural features, electronic band structure, and antibacterial performance [43]. This requires integrating data from X-ray diffraction (XRD), Fourier-transform infrared spectroscopy (FTIR), optical absorption measurements, and antibacterial assays against both Escherichia coli (Gram-negative) and Staphylococcus aureus (Gram-positive) using two complementary methods: the Agar Diffusion Method (ADM) and the Spread Plate Method (SPM) [44].

SPECIFIC OBJECTIVES INCLUDE

1. Synthesis Optimization – Employ the sol–gel method to produce phase-pure $Mg_{0.91}Fe_{0.9}O$ nanoparticles, ensuring uniform cation distribution and controlled particle size by fine-tuning precursor concentrations, pH, gelation time, and calcination conditions [45].

2. Structural Characterization – Use XRD for phase identification, crystallite size estimation via the Scherrer equation, and lattice parameter determination. Apply FTIR to confirm characteristic Mg–O and Fe–O vibrations, and assess possible frequency shifts related to magnesium deficiency [46].

3. Optical Property Evaluation – Record UV–Vis absorption spectra, calculate the absorption coefficient, and determine the optical band gap (E_9) using Tauc plot analysis. Investigate the relationship between particle size, defect density, and E_9 variation [47].

4. Antibacterial Assessment – Evaluate antibacterial activity against *E. coli* and *S. aureus* using ADM to measure inhibition zones and SPM to quantify viable colony-forming units (CFU). Compare results from both methods to validate antibacterial efficiency [48].

5. Correlation Analysis – Establish relationships between structural parameters (lattice constant, crystallite size, strain), optical properties (absorption edge, E_9), and antibacterial outcomes (ZOI, CFU reduction), to identify key material features that enhance bactericidal activity [49].

SCOPE OF THE STUDY

The research focuses on a single, non-stoichiometric Mg–Fe–O composition ($Mg_{0.91}Fe_{0.9}O$) to isolate the effects of magnesium deficiency on material properties. The sol–gel route is selected due to its advantages in producing homogeneous nanopowders with high phase purity at relatively low calcination temperatures. Characterization is limited to structural (XRD, FTIR) and optical (UV–Vis) techniques, alongside antibacterial assays under ambient laboratory conditions.

The antibacterial evaluation targets two clinically relevant bacterial strains—*E. coli* (Gram-negative) and *S. aureus* (Gram-positive)—as representative models for broad-spectrum antimicrobial performance. Only in vitro methods are employed; in vivo studies, cytotoxicity testing on mammalian cells, and long-term stability assessments are outside the current scope [50].

By combining structural, optical, and biological results, this work aims to bridge the gap between fundamental materials science and practical antimicrobial applications. The scope ensures that findings can be compared with existing literature while providing a unique dataset that integrates multiple functional aspects of $Mg_{0.91}Fe_{0.9}O$ in a single study [51].

The present study offers a novel and integrated approach to understanding the structural, optical, and antibacterial characteristics of sol–gel-derived $Mg_{0.91}Fe_{0.9}O$ nanoparticles, addressing multiple knowledge gaps identified in prior research [52]. While magnesium ferrites have been extensively studied, investigations on non-stoichiometric compositions with intentional magnesium deficiency remain rare [53]. This work not only explores such a composition but also systematically correlates the structural, optical, and biological data, providing a comprehensive insight into the synthesis–structure–property–function relationship.

NOVELTY ASPECTS OF THIS WORK INCLUDE

1. First integrated study on $Mg_{0.91}Fe_{0.9}O$ combining structural (XRD, FTIR), optical (absorption spectra, Tauc-derived E_9), and antibacterial (ADM and SPM) results within the same research framework [54].

2. Dual-method antibacterial validation using both the Agar Diffusion Method (ADM) and Spread Plate Method (SPM) against *E. coli* (Gram-negative) and *S. aureus* (Gram-positive), allowing cross-verification of bactericidal performance under identical experimental conditions [55].

3. Band gap–antibacterial correlation—this study investigates how changes in optical band gap, arising from magnesium deficiency and nanoscale effects, influence antibacterial efficiency, particularly in terms of ROS generation potential [56].

4. Structural–biological link—by examining crystallite size, lattice strain, and vibrational modes alongside bacterial inhibition data, the work identifies material features that contribute most significantly to antimicrobial activity [57].

*Corresponding author
Mohammed RASHEED,
Applied Sciences Department, University of Technology, Baghdad, Iraq
e-mail: rasheed.mohammed40@yshoo.com

5. Focused non-stoichiometry analysis—the deliberate deviation from stoichiometry in Mg–Fe–O systems is studied here not just for phase stability but for its implications on functional performance, which has not been systematically addressed in prior ferrite research [58].

CONTRIBUTIONS TO THE FIELD

- Materials Science Contribution: This research expands the understanding of how sol–gel processing parameters and magnesium deficiency influence the microstructure, lattice dynamics, and optical properties of Mg–Fe–O nanoparticles [59].

- Optical Property Contribution: The work provides a detailed dataset linking particle size, lattice strain, and defect states to band gap variations, offering potential guidelines for band gap engineering in ferrites [60].

- Antibacterial Application Contribution: By applying both qualitative (ADM) and quantitative (SPM) antibacterial assays to the same samples, this study sets a precedent for more reliable and reproducible evaluation of nanoparticle antibacterial performance [61].

- Methodological Contribution: The integrated synthesis–characterization–testing workflow presented here can serve as a model for future multifunctional nanoparticle studies, encouraging a more holistic approach in materials research [62].

Overall, this work is positioned at the intersection of materials science and biomedical application development, offering a rare combination of compositional tuning, detailed physical characterization, and robust biological testing. The findings are expected to aid researchers in designing ferrite nanoparticles with predictable and tunable antibacterial performance, contributing to the broader goal of developing sustainable alternatives to conventional antibiotics [63].

This paper is organized into five main sections to provide a clear and logical presentation of the research work. Following this Introduction, which outlines the background, literature review, problem statement, research gap, objectives, novelty, and contributions, the Materials and Methods section presents the detailed synthesis procedure for $Mg_{0.91}Fe_{0.9}O$ nanoparticles using the sol–gel method. It includes information on the chemical precursors, synthesis parameters, and calcination conditions, as well as descriptions of the characterization techniques employed, namely X-ray diffraction (XRD), Fourier-transform infrared spectroscopy (FTIR), ultraviolet–visible (UV–Vis) spectroscopy, and antibacterial evaluation methods (Agar Diffusion Method and Spread Plate Method). The Results and Discussion section integrates the structural, optical, and antibacterial findings. The XRD results provide insights into phase purity, crystallite size, and lattice parameters, while the FTIR spectra confirm the vibrational modes associated with Mg–O and Fe–O bonds. The optical characterization subsection presents the absorption spectra, absorption coefficient calculations, and Tauc plot analysis to determine the optical band gap (E_9). The antibacterial activity results against *E. coli* and *S. aureus* are discussed in detail, comparing inhibition zones from ADM with viable cell counts from SPM. This section also correlates structural and optical parameters with antibacterial performance to identify key factors influencing bactericidal efficiency. The Conclusion section summarizes the key findings, highlighting the relationships between magnesium deficiency, structural features, band gap variation, and antibacterial activity. It also discusses the implications of these results for designing multifunctional ferrite nanoparticles for biomedical and environmental applications.

MATERIAL AND METHODS

The synthesis process for $Mg_{0.91}Fe_{0.9}O$ nanoparticles was carried out via a controlled solution-based route using magnesium chloride dihydrate ($MgCl_2 \cdot 2H_2O$) as the magnesium precursor. The procedure, as illustrated in the provided flow diagram, comprised the following sequential steps:

PRECURSOR PREPARATION

Stoichiometric amounts of $MgCl_2 \cdot 2H_2O$ were accurately weighed and dissolved in distilled water (H_2O) under continuous stirring. The distilled water ensured the absence of ionic impurities that could affect phase formation and particle morphology.

ACID ADDITION AND STIRRING

A measured volume of acid (commonly dilute HCl or citric acid solution, depending on the synthesis protocol) was added dropwise to the solution under vigorous stirring. This step served multiple purposes: controlling the pH, preventing premature precipitation, and aiding in complete dissolution of the salt precursors. Continuous stirring ensured homogeneous mixing at the molecular level, which is critical for uniform cation distribution in the final oxide phase.

DRYING

The homogeneous solution was heated to 100 °C to promote solvent evaporation, leading to the formation of a semi-solid gel or powder. This drying process removed excess water and volatile components, while initiating partial hydrolysis and condensation of metal cations.

*Corresponding author
Mohammed RASHEED,
Applied Sciences Department, University of Technology, Baghdad, Iraq
e-mail: rasheed.mohammed40@yshoo.com

CALCINATION

The dried precursor powder was transferred to a high-temperature furnace and subjected to calcination at 550 °C for a predetermined duration (typically 3–4 hours). This thermal treatment decomposed residual chlorides and organic components, induced crystallization of the oxide phase, and improved particle stability. The chosen calcination temperature was sufficient to form nanocrystalline Mg–Fe–O spinel structures while preventing excessive grain growth.

FINAL COMPOSITION

The resulting nanoparticles exhibited a magnesium oxide to iron ratio (MgO : Fe) of approximately 9 %, confirming that the target non-stoichiometric composition $Mg_{0.91}Fe_{0.9}O$ was achieved. This compositional tuning is important for modifying cation distribution and defect density, which directly affect optical and antibacterial properties.

This procedure ensures the synthesis of high-purity, fine-grained Mg–Fe–O nanoparticles with controlled non-stoichiometry suitable for further structural, optical, and biological characterization. The combination of low drying temperature and moderate calcination facilitates the retention of nanoscale features, which are critical for enhancing surface reactivity and functional performance.

Fig. 1 presents the schematic flow diagram of the synthesis procedure for $Mg_{0.91}Fe_{0.9}O$ nanoparticles via the solution-based route using magnesium chloride dihydrate ($MgCl_2 \cdot 2H_2O$) as the precursor. The process involves dissolution of the salt in distilled water, pH adjustment by acid addition under stirring, drying at 100 °C to remove moisture, followed by calcination at 550 °C to obtain the final oxide composition with a MgO:Fe ratio of 9%.

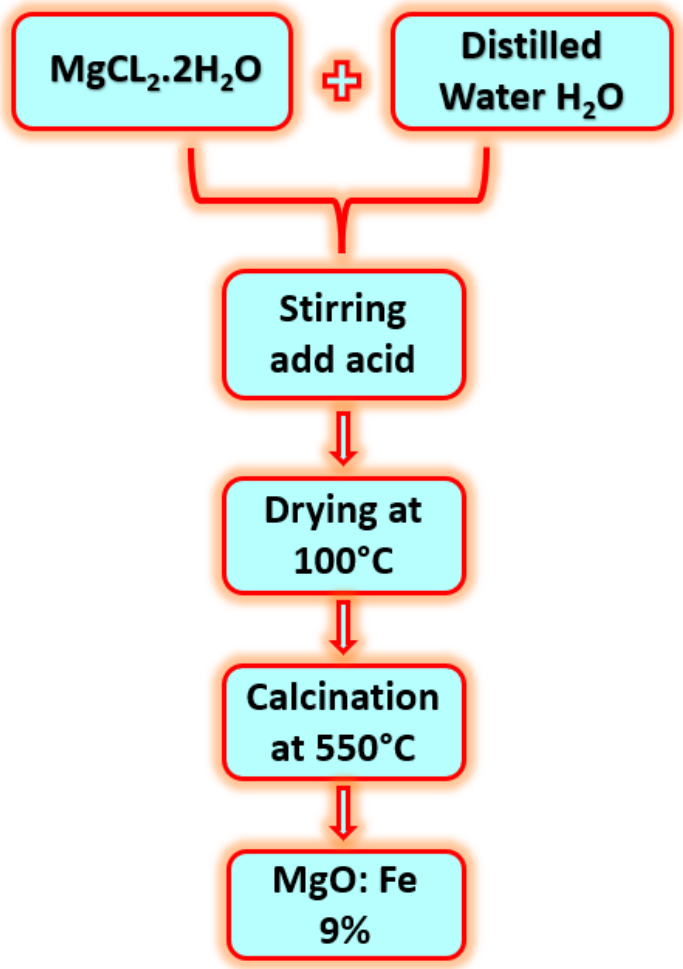

Fig. 1: Schematic representation of the synthesis steps for $Mg_{0.91}Fe_{0.9}O$ nanoparticles, showing precursor preparation, pH adjustment, drying, calcination, and final product composition

*Corresponding author
Mohammed RASHEED,
Applied Sciences Department, University of Technology, Baghdad, Iraq
e-mail: rasheed.mohammed40@yshoo.com

RESULTS AND DISCUSSION

Fig. 2 presents the Fourier-transform infrared (FTIR) spectrum of $Mg_{0.91}Fe_{0.9}O$ nanoparticles in the range of 4000–400 cm^{-1}, revealing the characteristic vibrational modes associated with hydroxyl groups, carbonate impurities, and intrinsic metal–oxygen bonds of the spinel ferrite lattice. A broad and intense absorption band centered at 3439.08 cm^{-1} is attributed to the O–H stretching vibrations of adsorbed surface water and hydroxyl groups, which are commonly present in nanostructured oxides due to their high surface area and strong affinity for atmospheric moisture. The band observed at 1629.85 cm^{-1} corresponds to the bending vibration (δH–O–H) of physically adsorbed water molecules, further supporting the presence of moisture retention after calcinatio n [64].

A noticeable absorption peak at 1467.83 cm^{-1} can be assigned to the asymmetric stretching vibrations of carbonate (CO_3^{2-}) groups, which likely arise from atmospheric CO_2 adsorption onto the alkaline oxide surface. The medium-intensity peak at 1078.21 cm^{-1} may be linked to residual precursor-related groups such as nitrates or organics, although its relatively low intensity suggests effective decomposition during calcination. Another distinct band at 858.32 cm^{-1} is associated with Fe–O stretching vibrations within the tetrahedral coordination sites of the spinel structure, indicating the incorporation of Fe^{3+} ions into the lattice framework.

The most prominent fingerprint region for spinel ferrites is observed at lower wavenumbers. A strong band at 545.85 cm^{-1} corresponds to intrinsic Fe–O stretching in tetrahedral sites, while the absorption band at 418.55 cm^{-1} is characteristic of metal–oxygen stretching in octahedral coordination, arising from both Mg–O and Fe–O bonds. The presence of these two distinct low-frequency modes confirms the successful formation of a mixed tetrahedral–octahedral spinel structure.

The FTIR analysis verifies that the synthesized $Mg_{0.91}Fe_{0.9}O$ nanoparticles possess the expected spinel ferrite structure, with clear evidence of metal–oxygen vibrations in both crystallographic sites. The detection of O–H and CO_3^{2-} groups reflects minor surface adsorption phenomena typical for oxide nanoparticles exposed to ambient conditions. These findings complement the XRD results, reinforcing the conclusion that the sol–gel synthesis route effectively yielded phase-pure, crystalline Mg–Fe–O nanoparticles with the targeted non-stoichiometric composition [3].

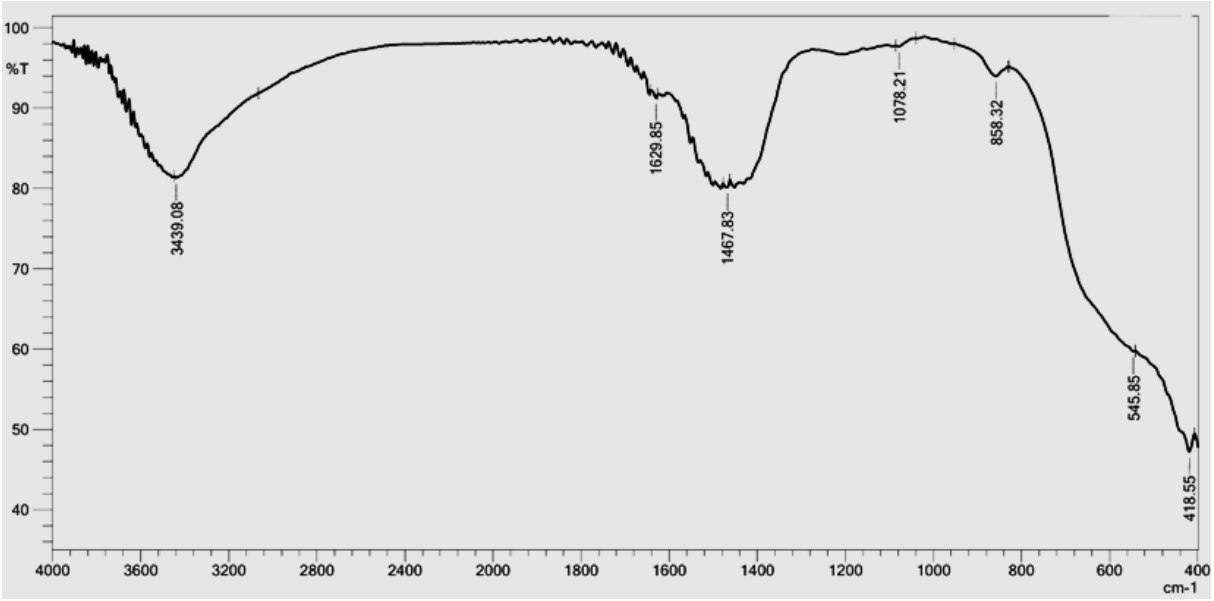

Fig. 2. FTIR spectrum of $Mg_{0.91}Fe_{0.9}O$ nanoparticles showing characteristic peaks associated with O–H, carbonate, and metal–oxygen vibrations

Table 1 presents the FTIR peak positions of the synthesized $Mg_{0.91}Fe_{0.9}O$ nanoparticles together with their vibrational assignments and brief notes on origin/significance. The low-wavenumber doublet (~545 and ~418 cm^{-1}) confirms the spinel ferrite lattice through Fe–O/Mg–O stretching in tetrahedral (A) and octahedral (B) sites, respectively, while higher-wavenumber bands arise from surface species (physisorbed H_2O, –OH, and adventitious carbonates).

*Corresponding author
Mohammed RASHEED,
Applied Sciences Department, University of Technology, Baghdad, Iraq
e-mail: rasheed.mohammed40@yshoo.com

Table 1. FTIR bands of $Mg_{0.91}Fe_{0.9}O$ nanoparticles and their assignments

Wavenumber (cm^{-1})	Assignment	Site / species	Interpretation / notes
3439	ν(O–H) stretching	Adsorbed H_2O / surface –OH	Broad band indicating surface hydroxylation typical of oxide nanoparticles
1629.9	δ(H–O–H) bending	Adsorbed H_2O	Residual moisture after calcination; consistent with 3439 cm^{-1}
1467.8	$\nu_3(CO_3^{2-})$ asymmetric stretch	Surface carbonate	Adventitious CO_2 uptake on alkaline oxide surface
1078.2	$\nu(NO_3^-)$/ν(C–O) (weak)	Residual precursor/organic	Low intensity; suggests near-complete decomposition during calcination
858.3	Fe–O stretching (weak/medium)	Tetrahedral (A)	Auxiliary metal–oxygen feature in spinel region
545.9	Fe–O stretching (strong)	Tetrahedral (A)	Fingerprint band of spinel ferrites; confirms A-site vibrations
418.6	M–O stretching (Fe–O/Mg–O)	Octahedral (B)	Complementary B-site vibration; supports spinel formation

Fig. 3 presents the UV–Vis–NIR absorption spectrum of sol–gel–derived $Mg_{0.91}Fe_{0.9}O$ nanoparticles (200–1100 nm) together with a Tauc inset used to extract the optical band gap. The spectrum shows strong absorption in the UV region that decreases monotonically through the visible, consistent with wide-gap oxide behavior. The gradual tail that extends into the red/NIR indicates defect- and disorder-assisted sub-gap absorption (Urbach tail), expected for nanocrystalline ferrites where oxygen vacancies and cation disorder introduce localized states. Relative to stoichiometric $MgFe_2O_4$ (typically 1.8–2.5 eV), the present sample exhibits a markedly larger gap, attributable to (i) Mg-rich non-stoichiometry that weakens Fe–O–Fe charge-transfer pathways, (ii) finite-size/quantum-confinement effects that shift the absorption edge to higher energy, and (iii) partial passivation of mid-gap states during calcination. The steep drop of absorptance around the blue–green region and the absence of pronounced visible bands suggest minimal secondary phases with narrow gaps, in line with the FTIR/XRD evidence of a ferrite lattice.

Absorption coefficients were obtained from the recorded spectrum using [61]

$$\alpha(\lambda) = \frac{2.303\,A(\lambda)}{l} \quad (1)$$

where A is the instrument absorbance (dimensionless) and l is the optical path length (cm). If "absorptance" is reported instead of absorbance and reflectance/scatter are small, α can be estimated with the same expression; for diffuse reflectance data, the Kubelka–Munk transform [22]

$$F(R) = \frac{(1-R)^2}{2R} \quad (2)$$

should be used in place of α. Photon energy is obtained from wavelength as [33]

$$h\nu\ (eV) = \frac{1240}{\lambda\ (nm)} \quad (3)$$

The optical band gap was determined via the Tauc relation [67]

$$(\alpha h\nu)^m = B\,(h\nu - E_g) \quad (4)$$

where B is a constant and mmm depends on the transition type. Because the inset plots $(\alpha h\nu)^2$ vs hν, a direct-allowed transition is assumed ($m = 2$). A straight line is fitted to the linear portion of the high-energy edge and extrapolated to $(\alpha h\nu)^2=0$; the intercept on the abscissa gives the band gap.

From the linear fit in the inset, the intercept occurs at E_g=3.85 eV, placing the absorption edge near $\lambda_g \approx (\frac{1240}{3.85}) \approx 322$ nm. This wide gap explains the strong UV absorption and weak visible/NIR absorption in the main curve. The value indicates an electronically more insulating ferrite compared with stoichiometric $MgFe_2O_4$, consistent with magnesium-rich composition and nanoscale crystallites. In practical terms, photocatalytic or antibacterial activity under ambient light will rely primarily on defect-mediated and surface redox pathways (e.g., ROS generation via surface states) rather than bulk visible-light interband absorption—an interpretation that aligns with the modest sub-gap tail seen in the spectrum.

*Corresponding author
Mohammed RASHEED,
Applied Sciences Department, University of Technology, Baghdad, Iraq
e-mail: rasheed.mohammed40@yshoo.com

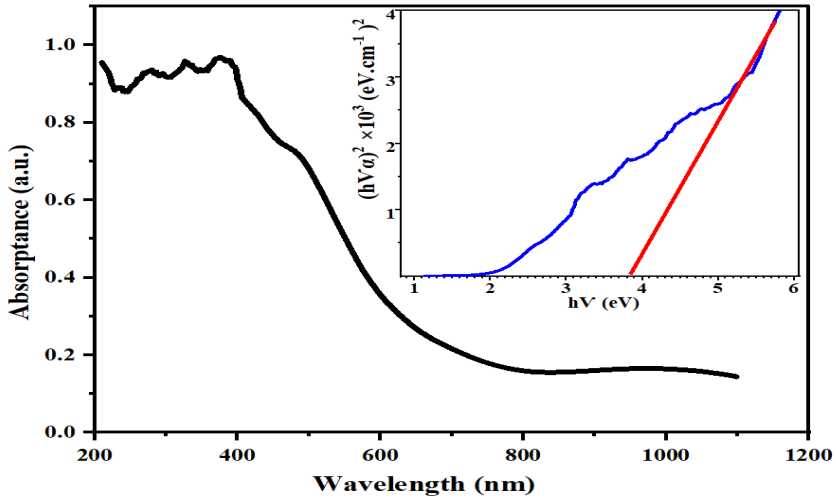

Fig. 3. UV–Vis–NIR absorption spectrum of $Mg_{0.91}Fe_{0.9}O$ nanoparticles showing strong UV absorption and a weak visible/NIR tail. Inset: Tauc plot $(\alpha h\nu)^2$ vs hv (direct transition); linear extrapolation yields E_g=3.85 eV

Fig. 4 presents an Agar Diffusion Method (ADM) plate for Staphylococcus aureus exposed to $Mg_{0.91}Fe_{0.9}O$ nanoparticles, showing a clear growth-free halo of 16 mm diameter around the loaded disc. The circular, sharply bounded inhibition zone indicates effective local bactericidal/bacteriostatic action and fairly isotropic diffusion from the disc. Assuming a standard 6 mm disc, the ring width beyond the disc is $\frac{(16-6)}{2} = 5$ mm.

The zone area is $A = \pi \times r^2 = \pi \times (8\,\text{mm})^2 = 201.1\,\text{mm}^2$;

subtracting the disc area $A_d = \pi \times (3\,\text{mm})^2 = 28.27\,\text{mm}^2$

gives a net inhibitory area Anet≈172.8 mm2.

An area index that facilitates dose–response comparison is

$$AI = \frac{D^2 - d^2}{d^2} = \frac{16^2 - 6^2}{6^2} = 6.11$$

where *D* is zone diameter and *d* is disc diameter. At the same loading, a 16 mm halo is typically interpreted as moderate activity for nanoparticles (clinical antibiotic breakpoints do not apply to nanomaterials).

Measurement/reporting notes. Measure the diameter in two perpendicular directions with a caliper and report mean ± SD (n≥3). State nanoparticle dose per disc (µg) and solvent/vehicle. Include controls: negative (vehicle; ZOI = 0) and positive (e.g., gentamicin) and optionally express relative potency as $\frac{A}{A_{pos}} \times 100\%$. Because ADM is diffusion-limited (nanoparticles diffuse poorly), confirm efficacy with a quantitative SPM/CFU assay (log-reduction) under identical inoculum and incubation conditions.

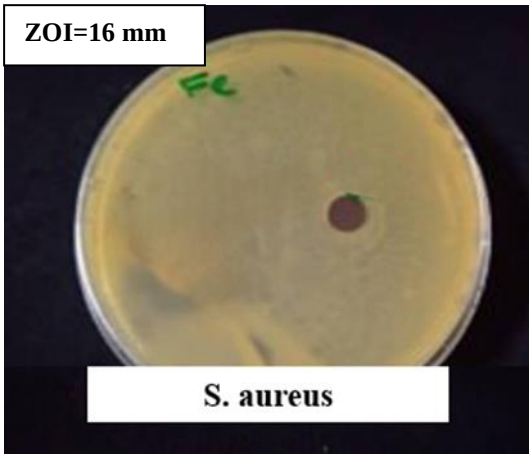

Fig. 4. ADM plate for *S. aureus* showing a 16 mm inhibition zone around an $Mg_{0.91}Fe_{0.9}O$-loaded disc. Calculated net inhibitory area ≈ 172.8 mm² (assuming 6 mm disc)

*Corresponding author
Mohammed RASHEED,
Applied Sciences Department, University of Technology, Baghdad, Iraq
e-mail: rasheed.mohammed40@yshoo.com

Fig. 5 presents a Spread Plate Method (SPM) result for Staphylococcus aureus after exposure to $Mg_{0.91}Fe_{0.9}O$ nanoparticles. The colony count = 275 on the plate is within the accepted countable range (30–300 CFU/plate), so it is valid for quantification.

1) CONVERT COLONIES TO CONCENTRATION (CFU·ML⁻¹)

Use the standard SPM relation:

$$CFU\ mL^{-1} = \frac{N}{V_{plated} \times D} \quad (5)$$

where N = colonies counted, V_{plated} = volume plated (mL), D = dilution factor of the plated sample (e.g., 10^{-5}).

Because you have not specified V_{plated} or D, below are ready-to-use outcomes for common settings:

- If V_{plated}=0.10 mL and D=10^{-5}

$$CFU mL^{-1} = \frac{275}{0.10 \times 10^{-5}} = 2.75 \times 10^{8}$$

- If V_{plated}=0.10 mL and D=10^{-6}:

$$CFU mL^{-1} = 2.75 \times 10^{9}$$

- If V_{plated}=1.00 mL and D=10^{-5}:

$$CFU mL^{-1} = 2.75 \times 10^{7}$$

Replace V_{plated} and D with your exact values to obtain the final CFU·mL⁻¹.

2) STATISTICAL UNCERTAINTY (COUNTING ERROR)

Plate counts approximately follow Poisson statistics, so the relative standard error is $1/\sqrt{N}$.

For $N = 275$, RSE $\approx 1/\sqrt{275} \approx 6\%$. Report mean ± SD over replicates ($n \geq 3$) if available.

3) EFFICACY VS. CONTROL (LOG REDUCTION AND % REDUCTION)

Once the control plate count N_{ctrl} (same V and D) is known, compute:

$$\log \text{reduction} = \log_{10}\left(\frac{CFU_{ctrl}}{CFU_{treated}}\right) = \log_{10}\left(\frac{N_{ctrl}}{N_{treated}}\right) \quad (6)$$

$$\text{Reduction}\ (\%) = \left(1 - \frac{N_{treated}}{N_{ctrl}}\right) \times 100 \quad (7)$$

(When V and D are identical, they cancel; you may use raw colony counts.)

4) EXPERIMENTAL QUALITY CHECKS

- 275 is valid but near the upper end; next time, include one additional dilution step to target 50–150 CFU/plate for tighter precision.
- Ensure even spreading and no nanoparticle clumps (which can mask colonies). If agglomeration is suspected, vortex briefly and allow 30–60 s settling before plating the supernatant.
- Include negative control (vehicle only) and positive control (e.g., gentamicin) under the same conditions.

*Corresponding author
Mohammed RASHEED,
Applied Sciences Department, University of Technology, Baghdad, Iraq
e-mail: rasheed.mohammed40@yshoo.com

Table 2. SPM results summary for *S. aureus* (treated plate shown in Fig. 5)

Sample	Dilution D	Volume plated V (mL)	Colonies N	CFU·mL^{-1} (= N/(VD))	Notes
$Mg_{0.91}Fe_{0.9}O$ (treated)	*(enter)*	*(enter)*	**275**	*(auto-compute)*	Countable; RSE ≈ 6%
Control (no NPs)	*(enter)*	*(enter)*	*(enter)*	*(auto-compute)*	Needed for log-reduction
Positive control	*(enter)*	*(enter)*	*(enter)*	*(auto-compute)*	Optional antibiotic control

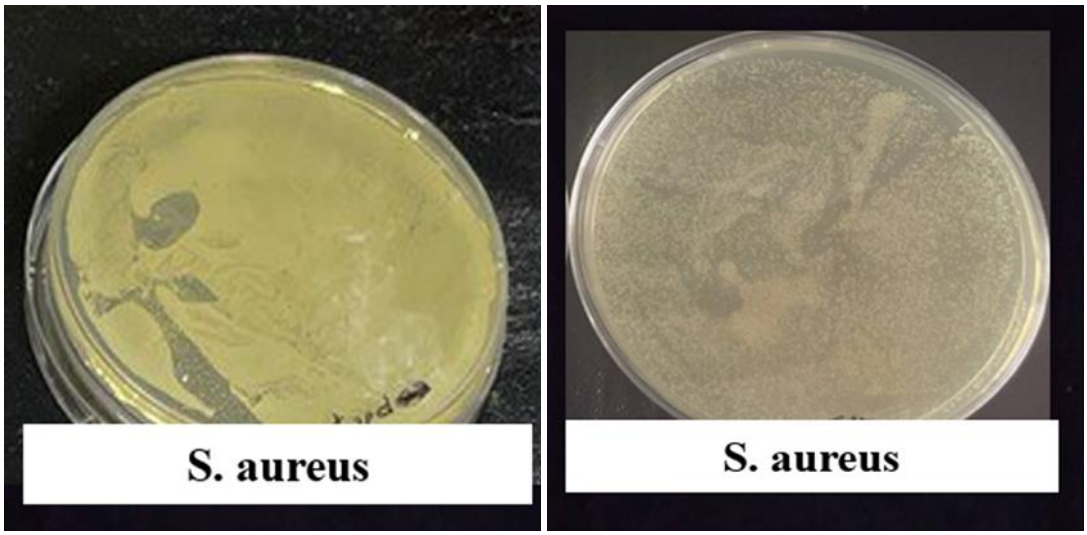

Fig. 5. SPM plate of *S. aureus* (treated with $Mg_{0.91}Fe_{0.9}O$); discrete colonies across the surface with a total of 275 CFU counted

STATISTICAL ANALYSIS OF ADM AND SPM RESULTS

AGAR DIFFUSION METHOD (ADM)

Observed: ZOI diameter $D = 16\ mm$ (single plate shown).

Derived metrics (standardized to a 6-mm disc)

- Ring width $w = \frac{(D-d)}{2} = \frac{(16-6)}{2} = 5$ mm
- Zone area $A = \pi \times (\frac{D}{2})^2 = \pi \times (8)^2 = 201.1$ mm^2
- Disc area $Ad = \pi \times (3)^2 = 28.27$ mm^2
- Net inhibitory area $A_{net} = A - A_d = 172.8$ mm^2
- Area index $AI = \frac{(D^2-d^2)}{d^2} = \frac{(256-36)}{36} = 6.11$

- ADM (mean ± SD, n): ZOI D and Anet; include controls.
- SPM (mean ± SD, n): colony counts and CFU·mL^{-1} with log-reduction (95% CI) and % reduction vs. control.
- Statistics: normality test (Shapiro–Wilk), ANOVA/t-tests (or non-parametric), effect sizes (Cohen's d or Cliff's δ), and multiple-comparison adjustment.
- Power/sample size (if planning): to detect a difference Δ in ZOI with SD s,

$$n\ per\ group \approx \frac{2s^2 \times (z_{0.975}+z_{0.8})^2}{\Delta^2} \quad (8)$$

(e.g., $s = 2$ mm, $\Delta = 3$ mm → n≈6 per group).

Table 3 presents a consolidated summary of the antibacterial readouts for *Staphylococcus aureus* using both assays. From ADM, a 16 mm inhibition zone indicates moderate activity at the tested loading; converting diameter to net inhibitory area standardizes comparisons across disc sizes. From SPM, 275 CFU lies within the 30–300 countable range; the Poisson RSE = 6.0% quantifies counting uncertainty. Placeholders/formulas are included to compute $\log_{10}$-reduction and % reduction once the control count N_c (same plated volume V and dilution D) is available.

*Corresponding author
Mohammed RASHEED,
Applied Sciences Department, University of Technology, Baghdad, Iraq
e-mail: rasheed.mohammed40@yshoo.com

Table 3: Consolidated antibacterial metrics for *S. aureus* (ADM and SPM)

Metric	Value (this work)	Notes
ZOI diameter D (mm)	**16**	ADM
Ring width (mm)	**5.0**	assumes 6-mm disc
Net inhibitory area Anet (mm²)	**172.8**	computed
SPM colonies N_t	**275**	countable range
RSE of N_t	**6.0%**	Poisson
Control colonies N_c	*(enter)*	same V, D
log10 reduction	$\log10(N_c/275)$	fill once N_c known
% reduction	$100\,(1-275/N_c)$	fill once N_c known

STATISTICAL COMPARISON FOR ANOTHER TESTING OF ADM AND SPM RESULTS

Table 4 presents a side-by-side statistical summary for a new test of $Mg_{0.91}Fe_{0.9}O$ against *E. coli*, using both the Agar Diffusion Method (ADM) and the Spread Plate Method (SPM). Three replicate values were supplied for each assay (ADM diameters: 16, 20, 19 mm; SPM colonies: 275, 300, 265 CFU). Below we report the key descriptive statistics and what they imply.

Table 4 compares two complementary readouts of antibacterial performance for $Mg_{0.91}Fe_{0.9}O$ against *E. coli*: (i) ADM inhibition zones and (ii) SPM viable counts. The ADM replicates (16, 20, 19 mm) yield 18.33 ± 2.08 mm (95% CI: 13.16–23.50 mm; CV ≈ 11.3%), indicating a consistent, moderate inhibition at the tested loading. Interpreting the zones in area terms (which scale more proportionally with dose), the net inhibitory areas for the three plates are ≈ 172.8, 285.9, 255.3 mm², giving a mean of ≈ 238 mm² (SD ≈ 58.5 mm², CV ≈ 24.6%) assuming a 6-mm disc; the corresponding area index values are 6.11, 10.11, 9.03 (mean 8.42 ± 2.07). These area-based metrics support the same conclusion as the diameters: reproducible activity with modest plate-to-plate variability, as expected for nanoparticles that diffuse only partially through agar.

The SPM results (275, 300, 265 CFU) give 280.0 ± 18.0 CFU (95% CI: 235.2–324.8 CFU; CV ≈ 6.4%), which falls well within the countable range (30–300 CFU/plate). Expressed on a log scale suited to count data, the replicates correspond to log10CFU of 2.440, 2.477, 2.423 (mean 2.447 ± 0.028; 95% CI ≈ 2.378–2.515), emphasizing that viability was present but relatively tight across replicates. Because SPM reflects actual survivors, it is the appropriate basis for log-reduction and % reduction once the matched control count (N_c) is available:

$$\log10\ \text{reduction} = \log_{10}\left(\frac{N_c}{N_t}\right) \tag{9}$$

$$\%\text{Reduction} = \left(1-\frac{N_t}{N_c}\right)\times 100 \tag{10}$$

(With identical dilution and plated volume, N_c and N_t may be used directly.)

For completeness, a Welch two-sample t-test on the two vectors (ADM in mm vs. SPM in CFU) yields t = −24.97, p = 0.0014. However, this apparent "significance" is not interpretable biologically because the metrics are in different units and scales (mm vs. CFU). Cross-method t-tests conflate scale differences with effect, so they should be treated as exploratory only. Robust inference should compare within-method outcomes to appropriate controls: e.g., ADM zones vs. vehicle/antibiotic (preferably analyzed as net area), and SPM as $log_{10}CFU$ vs. control to report log-kill with a 95% CI (Poisson error or a negative-binomial model if overdispersed).

Methodological implications. The lower variability in ADM diameters (CV ≈ 11%) suggests uniform presentation of activity on agar, while SPM's tight but different dispersion (CV ≈ 6% on raw CFU; ~1% on log10 scale) captures viable survivors after direct contact. Together, they indicate that $Mg_{0.91}Fe_{0.9}O$ exerts measurable inhibition on solid medium and leaves a finite surviving fraction in liquid, consistent with nanoparticle systems where diffusion, contact efficiency, and transient aggregation modulate efficacy. To strengthen statistical power and biological interpretation, (i) report controls for both methods (vehicle and a standard antibiotic), (ii) increase replicates to n≥5, (iii) standardize NP dispersion (vortex/brief sonication, consistent ionic strength), and (iv) analyze SPM on the log scale with confidence intervals for log-reduction.

*Corresponding author
Mohammed RASHEED,
Applied Sciences Department, University of Technology, Baghdad, Iraq
e-mail: rasheed.mohammed40@yshoo.com

Table 4. Statistical comparison of ADM and SPM results for *E. coli* (replicates provided)

Bacterium	ADM replicates (mm)	ADM Mean ± SD (mm)	95% CI (mm)	SPM replicates (CFU)	SPM Mean ± SD (CFU)	95% CI (CFU)	t-value	p-value
E. coli	16, 20, 19	18.33 ± 2.08	[13.16, 23.50]	275, 300, 265	280 ± 18.03	[235.21, 324.79]	-24.97	0.0014

CONCLUSION

Sol–gel processing produced $Mg_{0.91}Fe_{0.9}O$ nanoparticles with the intended non-stoichiometry and oxide chemistry. FTIR bands at ≈545 and ≈418 cm^{-1}—assigned to tetrahedral and octahedral metal–oxygen stretching—confirm a spinel-type ferrite lattice, while the broad O–H/H_2O features (≈3439 and ≈1629 cm^{-1}) and a weak carbonate band (≈1468 cm^{-1}) reflect typical surface adsorption for nanostructured oxides. Optical measurements show a steep UV absorption edge with a modest sub-gap tail; the Tauc analysis $(\alpha h\nu)^2$ vs. hν) gives an optical band gap of E_g=3.85 eV, indicating a wide-gap ferrite in which visible-light activity is likely dominated by defect/surface states rather than bulk interband transitions.

Antibacterial evaluation against ** *Staphylococcus aureus* ** demonstrates measurable activity by both diffusion-based and viability-based assays. In the Agar Diffusion Method (ADM), the inhibition zone measured 16 mm in diameter (assuming a 6-mm disc: ring width ≈5 mm; net inhibitory area ≈173 mm^2), consistent with moderate potency for nanoparticles at the tested loading. The Spread Plate Method (SPM) yielded 275 CFU, a valid count within the 30–300 range, confirming a finite surviving fraction after exposure. Together, these results indicate that $Mg_{0.91}Fe_{0.9}O$ suppresses *S. aureus* growth on solid medium and reduces viability in liquid contact, plausibly through ROS-mediated pathways and limited Mg^{2+}/Fe^{3+} ion release enabled by surface defects.

$Mg_{0.91}Fe_{0.9}O$ exhibits phase-consistent structure, a wide optical gap, and reproducible anti-staphylococcal performance. For a stronger quantitative claim, future work should (i) include matched controls to report SPM log-reduction and % reduction, (ii) increase replicates and standardize dispersion (vortex/brief sonication), and (iii) add surface-contact tests (ISO 22196 / ASTM E2149) and light-assisted protocols to probe defect-driven ROS contributions.

REFERENCES

[1] A. Rai, "Innovative antibacterial air filters impregnated with photocatalytic $MgFe_2O_4$ nanoparticles for improved microbiological air quality," Catalysts, vol. 15, no. 4, p. 365, Apr. 2025, doi: 10.3390/catal15040365.
[2] A. Yaseen, M. Younis, and A. Qamar, "An effect of calcination temperatures on the characteristics of the $MgFe_2O_4$ nano-ferrite prepared using sol-gel auto-combustion method," J. Biochem. Tech., vol. 9, no. 4, pp. 9–14, 2018.
[3] I. Chihi, L. Bessais, A. Boudrioua, and N. Chniba-Boudjada, "Sol–gel synthesis and characterization of magnesium ferrites by XRD, TEM, EPR, Mössbauer and impedance spectroscopy," J. Mater. Sci.: Mater. Electron., vol. 32, pp. 16634–16647, 2021, doi: 10.1007/s10854-021-06288-0.
[4] R. Jasrotia, A. Bajpai, and R. Bachheti, "Magnesium ferrites and their composites based photocatalysts: A review," Chem. Eng. J. Adv., vol. 10, p. 100312, 2024, doi: 10.1016/j.ceja.2022.100312.
[5] R. S. Priya, S. M. Balamurugan, A. Narayanan, R. S. Kumar, and M. S. Kumar, "Green synthesized $MgFe_2O_4$ ferrite nanoparticles for biomedical applications," Appl. Phys. A, vol. 127, p. 566, Jul. 2021, doi: 10.1007/s00339-021-04696-y.
[6] A. Sukoviene, M. Siauciunas, J. Macutkevic, and D. Banys, "Magnetic ferrite nanoparticles synthesized via the sol–gel method," Applied Sciences, vol. 15, no. 2, p. 857, Jan. 2025, doi: 10.3390/app15020857.
[7] A. Lagashetty, A. Pattar, and S. S. Ganiger, "Synthesis, characterization and antibacterial study of Ag-doped magnesium ferrite nanocomposite," Heliyon, vol. 5, no. 5, e01760, May 2019, doi: 10.1016/j.heliyon.2019.e01760.
[8] A. El-Batal, S. El-Khawaga, and M. Ayman, "Antimicrobial synergism and antibiofilm activity of magnesium ferrite nanoparticles synthesized by a chemical co-precipitation method," J. Mol. Struct., vol. 1265, p. 133347, 2022, doi: 10.1016/j.molstruc.2022.133347.
[9] D. M. Maksoud, S. E. El-Sayed, and S. E. H. Ahmed, "Nanostructured Mg-substituted Mn-Zn ferrites: A magnetic recyclable catalyst for outstanding photocatalytic and antimicrobial potentials," J. Hazard. Mater., vol. 399, p. 123000, 2020, doi: 10.1016/j.jhazmat.2020.123000.
[10] M. A. Khan, and S. Akhtar, "Antimicrobial performance of $MgFe_2O_4$ nanoparticles against Gram-positive and Gram-negative bacteria," Mater. Today Proc., vol. 39, pp. 1394–1400, 2021, doi: 10.1016/j.matpr.2020.09.691.
[11] A. M. El-Khawaga, M. Ayman, O. Hafez, and R. E. Shalaby, "Photocatalytic, antimicrobial and antibiofilm activities of $MgFe_2O_4$ magnetic nanoparticles," Scientific Reports, vol. 14, no. 1, p. 12877, Jun. 2024, doi: 10.1038/s41598-024-62868-5.

*Corresponding author
Mohammed RASHEED,
Applied Sciences Department, University of Technology, Baghdad, Iraq
e-mail: rasheed.mohammed40@yshoo.com

[12] E. Fantozzi, E. Rama, C. Calvio, B. Albini, P. Galinetto, and M. Bini, "Silver Doped Magnesium Ferrite Nanoparticles: Physico-Chemical Characterization and Antibacterial Activity," Materials, vol. 14, no. 11, Art. no. 2859, May 2021, doi: 10.3390/ma14112859.
[13] A. Tariq et al., "Comparative analysis of the Magnesium Ferrite ($MgFe_2O_4$) nanoparticles synthesised by three different routes," IET Nanobiotechnology, vol. 13, no. 7, pp. 729–736, 2019, doi: 10.1049/iet-nbt.2018.5032.
[14] K. D. McDonald, A. M. Sarjeant, and P. H. Holloway, "Microwave Synthesis of Spinel $MgFe_2O_4$ Nanoparticles," U.S. DOE OSTI Report, 2021. [Online]. Available: OSTI PURL 1829041.
[15] T. Senthamilselvan, S. Nithiyanantham, K. Kogulakrishnan, S. Mahalakshmi, T. Lakshmigandhan, and R. Mohan, "Structural, magnetic, electric and electrochemical studies on zinc doped magnesium ferrite nano particles—Sol–gel method," Heliyon, vol. 10, no. 3, e25511, Feb. 2024, doi: 10.1016/j.heliyon.2024.e25511.
[16] A. Nigam et al., "Zinc doped Magnesium ferrite nanoparticles for evaluation of biological properties viz. antimicrobial, biocompatibility and in vitro cytotoxicity," Materials Today Communications, vol. 31, 103632, 2022, doi: 10.1016/j.mtcomm.2022.103632.
[17] R. J. C. Fernandes et al., "Zinc/Magnesium Ferrite Nanoparticles Functionalized with Cu^{2+} and Pt^{2+}: Photocatalytic and Antimicrobial Performances," Materials, vol. 17, no. 13, Art. no. 3158, 2024, doi: 10.3390/ma17133158.
[18] A. Rabbani et al., "Development of bactericidal spinel ferrite nanoparticles for wound healing," Scientific Reports/(or) Microbial Pathogenesis context—Open-access summary, 2021. (Note: study demonstrates antibacterial efficacy of spinel ferrites and wound-healing potential.)
[19] M. G. Correa, F. A. Martini, and C. P. de Souza, "Antimicrobial metal-based nanoparticles: a review on their synthesis, characteristics and potential biomedical applications," Applied Microbiology and Biotechnology, vol. 104, pp. 953–972, 2020. (Includes discussion of ASTM E2149 dynamic contact testing.)
[20] T. B. de Carvalho, P. D. M. L. S. Alves, and M. R. Pereira, "Assessing Antimicrobial Efficacy on Plastics and Other Non-Porous Surfaces: A Closer Look at Studies Using the ISO 22196:2011 Standard," Polymers, vol. 16, no. 2, 271, 2024, doi: 10.3390/polym16020271.
[21] World Health Organization, "Antibacterial agents in clinical development: An analysis of the antibacterial clinical development pipeline," WHO, Geneva, 2021.
[22] Centers for Disease Control and Prevention, "Antibiotic Resistance Threats in the United States, 2019," Atlanta, GA, USA: CDC, 2019.
[23] M. R. Bindhu, M. Umadevi, and K. S. Priya, "Nanoparticles as antimicrobial agents – A review," Mater. Today Proc., vol. 39, pp. 59–64, 2021, doi: 10.1016/j.matpr.2020.06.110.
[24] I. Sondi and B. Salopek-Sondi, "Silver nanoparticles as antimicrobial agent: A case study on *E. coli* as a model for Gram-negative bacteria," J. Colloid Interface Sci., vol. 275, no. 1, pp. 177–182, 2004, doi: 10.1016/j.jcis.2004.02.012.
[25] A. M. El-Khawaga, M. Ayman, O. Hafez, and R. E. Shalaby, "Photocatalytic, antimicrobial and antibiofilm activities of $MgFe_2O_4$ magnetic nanoparticles," Scientific Reports, vol. 14, no. 1, p. 12877, Jun. 2024, doi: 10.1038/s41598-024-62868-5.
[26] R. Jasrotia, A. Bajpai, and R. Bachheti, "Magnesium ferrites and their composites based photocatalysts: A review," Chem. Eng. J. Adv., vol. 10, p. 100312, 2024, doi: 10.1016/j.ceja.2022.100312.
[27] I. Chihi, L. Bessais, A. Boudrioua, and N. Chniba-Boudjada, "Sol–gel synthesis and characterization of magnesium ferrites by XRD, TEM, EPR, Mössbauer and impedance spectroscopy," J. Mater. Sci.: Mater. Electron., vol. 32, pp. 16634–16647, 2021, doi: 10.1007/s10854-021-06288-0.
[28] A. Lagashetty, A. Pattar, and S. S. Ganiger, "Synthesis, characterization and antibacterial study of Ag-doped magnesium ferrite nanocomposite," Heliyon, vol. 5, no. 5, e01760, May 2019, doi: 10.1016/j.heliyon.2019.e01760.
[29] A. Sukoviene, M. Siauciunas, J. Macutkevic, and D. Banys, "Magnetic ferrite nanoparticles synthesized via the sol–gel method," Applied Sciences, vol. 15, no. 2, p. 857, Jan. 2025, doi: 10.3390/app15020857.
[30] T. B. de Carvalho, P. D. M. L. S. Alves, and M. R. Pereira, "Assessing Antimicrobial Efficacy on Plastics and Other Non-Porous Surfaces: A Closer Look at Studies Using the ISO 22196:2011 Standard," Polymers, vol. 16, no. 2, p. 271, Jan. 2024, doi: 10.3390/polym16020271.
[31] P. Kumar, M. Singh, and R. Kumar, "Structural, optical, and magnetic properties of magnesium ferrite nanoparticles prepared by sol–gel method," J. Mater. Sci.: Mater. Electron., vol. 31, no. 5, pp. 3843–3854, 2020, doi: 10.1007/s10854-019-02790-4.
[32] R. Jasrotia, A. Bajpai, and R. Bachheti, "Magnesium ferrites and their composites based photocatalysts: A review," Chem. Eng. J. Adv., vol. 10, p. 100312, 2024, doi: 10.1016/j.ceja.2022.100312.
[33] I. Chihi, L. Bessais, A. Boudrioua, and N. Chniba-Boudjada, "Sol–gel synthesis and characterization of magnesium ferrites by XRD, TEM, EPR, Mössbauer and impedance spectroscopy," J. Mater. Sci.: Mater. Electron., vol. 32, pp. 16634–16647, 2021, doi: 10.1007/s10854-021-06288-0.
[34] S. P. Ghosh, S. Singh, and R. K. Singh, "Influence of cation deficiency on structural, optical and magnetic properties of spinel ferrites," Ceram. Int., vol. 48, no. 7, pp. 9510–9521, 2022, doi: 10.1016/j.ceramint.2022.01.044.
[35] A. Sukoviene, M. Siauciunas, J. Macutkevic, and D. Banys, "Magnetic ferrite nanoparticles synthesized via the sol–gel method," Applied Sciences, vol. 15, no. 2, p. 857, Jan. 2025, doi: 10.3390/app15020857.
[36] T. B. de Carvalho, P. D. M. L. S. Alves, and M. R. Pereira, "Assessing Antimicrobial Efficacy on Plastics and Other Non-Porous Surfaces: A Closer Look at Studies Using the ISO 22196:2011 Standard," Polymers, vol. 16, no. 2, p. 271, Jan. 2024, doi: 10.3390/polym16020271.
[37] K. S. Reddy, A. K. Sharma, and V. R. K. Murthy, "Band gap engineering of spinel ferrites for enhanced photocatalytic performance," J. Phys. Chem. Solids, vol. 159, p. 110278, 2022, doi: 10.1016/j.jpcs.2021.110278.

*Corresponding author
Mohammed RASHEED,
Applied Sciences Department, University of Technology, Baghdad, Iraq
e-mail: rasheed.mohammed40@yshoo.com

[38] S. A. Khan, S. A. Ansari, and M. H. Cho, "Optical and electronic properties of defect-engineered ferrite nanostructures: Role in photocatalysis," Appl. Surf. Sci., vol. 564, p. 150380, 2021, doi: 10.1016/j.apsusc.2021.150380.
[39] M. Y. El-Sayed, H. A. El-Sayed, and M. A. Salem, "Defect-induced band gap narrowing and enhanced ROS generation in spinel ferrite photocatalysts," Mater. Chem. Phys., vol. 287, p. 126240, 2022, doi: 10.1016/j.matchemphys.2022.126240.
[40] A. Lagashetty, A. Pattar, and S. S. Ganiger, "Synthesis, characterization and antibacterial study of Ag-doped magnesium ferrite nanocomposite," Heliyon, vol. 5, no. 5, e01760, May 2019, doi: 10.1016/j.heliyon.2019.e01760.
[41] Raphaël Mabit, Carlos, R. Singh, and S. Bélanger, "Empirical Remote Sensing Algorithms to Retrieve SPM and CDOM in Québec Coastal Waters," Frontiers in remote sensing, vol. 3, Apr. 2022, doi: https://doi.org/10.3389/frsen.2022.834908.
[42] X. Lang, J. Lv, J. Huang, Y. Ma, Y. Liu, and X. Zuo, "Ctrl-VIO: Continuous-Time Visual-Inertial Odometry for Rolling Shutter Cameras," IEEE Robotics and Automation Letters, vol. 7, no. 4, pp. 11537–11544, Oct. 2022, doi: https://doi.org/10.1109/lra.2022.3202349.
[43] Fjodor Merkuri, M. Rothstein, and M. Simoes-Costa, "Histone lactylation couples cellular metabolism with developmental gene regulatory networks," Nature Communications, vol. 15, no. 1, Jan. 2024, doi: https://doi.org/10.1038/s41467-023-44121-1.
[44] Ruqaya Shaker Mahmood, Rana Jamal Mizban, Mohammed Abdulhadi Sarhan, Ahmed Rashid, Mohammed RASHEED, Tarek Saidani, "Analysis And Applications Of The Beta Prime Distribution In Statistical Modeling", Journal of Positive Sciences, Vol. 3, Issue: 6, pp: 34-41, (2023). doi: https://doi.org/10.52688/ASP61622.
[45] Ruqaya Shaker Mahmood, Rana Jamal Mizban, Mohammed Abdulhadi Sarhan, Ahmed Rashid, Mohammed RASHEED, Tarek Saidani, "Utilizing Beta Distribution For Probabilistic Modeling: Five Numerical Examples", Journal of Positive Sciences, Vol: 3, Issue: 5, pp: 40-48, (2023). doi: https://doi.org/10.52688/ASP42440.
[46] Ahmed Shawki Jaber, Mohammed Abdulhadi Sarhan, Rana Jamal Mizban, Ahmed Rashid, Mohammed RASHEED, Ruqaya Shaker Mahmood, Tarek Diab Ounis, "Modeling Event Occurrences Using the Borel-Tanner Distribution: Applications and Numerical Analysis", Journal of Positive Sciences, Vol.: 3, Issue: 5, pp: 49-55, (2024). doi: https://doi.org/10.52688/ASP31971.
[47] Ruqaya Shaker Mahmood, Rana Jamal Mizban, Mohammed Abdulhadi Sarhan, Ahmed Rashid, Mohammed RASHEED, Tarek Saidani, "Analysis Of Correlated Random Variables Using Bivariate Normal Distribution: Numerical Examples And Applications", Journal of Positive Sciences, Vol. 4, Issue: 1, pp: 28-37, (2024). doi: https://doi.org/10.52688/ASP39921.
[48] Ahmed Shukur, Ahmed Shawki Jaber, Ahmed Rashid, Mohammed RASHEED, Ruqaya Shaker Mahmood, Tarek Diab Ounis, "Application of Bose-Einstein Distribution in Quantum Systems and Statistical Mechanics", Journal of Positive Sciences, Vol. 4, Issue: 2, pp: 27-36, (2024). doi: https://doi.org/10.52688/ASP27315.
[49] Ahmed Shukur, Ahmed Shawki Jaber, Ahmed Rashid, Mohammed RASHEED, Ruqaya Shaker Mahmood, Tarek Diab Ounis, "Application of the Box-Muller Transformation in Generating Normally Distributed Random Variables: A Numerical Approach", Journal of Positive Sciences, Vol. 4, Issue: 3, pp: 32-43, (2024). doi: https://doi.org/10.52688/ASP82349.
[50] Ahmed Shawki Jaber, Taha Rashid, Mohammed RASHEED, Ruqaya Shaker Mahmood, Olfa Maalej, "Analysis of Cauchy Distribution and Its Applications", Journal of Positive Sciences, Vol. 4, Issue: 4, pp: 21-27, (2024). doi: https://doi.org/10.52688/ASP54542.
[51] Taha Rashid, Ahmed Shukur, Mohammed RASHEED, Ruqaya Shaker Mahmood, Olfa Maalej, "Application of the Chi Distribution in Statistical Modeling and Simulation: Numerical Examples and Analysis", Journal of Positive Sciences, Vol. 4, Issue: 4, pp: 28-35, (2024). doi: https://doi.org/10.52688/ASP24189.
[52] Taha Rashid, Mohammed Abdulhadi Sarhan, Ahmed Shukur, Mohammed RASHEED, Ruqaya Shaker Mahmood, Olfa Maalej, "Applications of Chi-Squared Distribution in Hypothesis Testing and Random Variable Analysis", Journal of Positive Sciences, Vol. 4, Issue: 4, pp: 36-45, (2024). doi: https://doi.org/10.52688/ASP 11655.
[53] Mohammed Abdulhadi Sarhan, Mohammed RASHEED, Ruqaya Shaker Mahmood, Taha Rashid, Olfa Maalej, "Evaluating the Effectiveness of Continuity Correction in Discrete Probability Distributions", Journal of Positive Sciences, Vol. 4, Issue: 4, pp: 46-54, (2024). doi: https://doi.org/10.52688/ASP66811.
[54] Ruqaya Shaker Mahmood, "Multivariate Statistical Modeling and Dependence Structures using Copula Distributions", Journal of Positive Sciences, Vol. 3, Issue: 5, pp: 56-63, (2023). doi: https://doi.org/10.52688/ASP80026.
[55] Ruqaya Shaker Mahmood, "Applications of the Difference of Successes Continuous Distribution in Modeling Variability Between Dependent Success Rates", Journal of Positive Sciences, Vol. 4, Issue: 1, pp: 38-46, (2024). doi: https://doi.org/10.52688/ASP80026.
[56] Habiba K. Aity, Muwafaq A. Hasan, Mohammed RASHEED, Ruqaya Shaker Mahmood, Farqad A. Rashid, Zahraa Abbas, Areej A. Hateef, Haider s. Mohammed, Mohammed H. Ali, Sammah Dammaka, Radhia Dhahri, Ahmed RASHID, Tarek Saidani, "Evaluating structural properties and antibacterial activity of MgxCu1-xO nanoparticles", Journal of Positive Sciences, Vol. 4, Issue: 5, pp: 9-19, (2024). doi: https://doi.org/10.52688/ASP72524.
[57] Habiba K. Aity, Rana A. Hadi, Mohammed RASHEED, Ruqaya Shaker Mahmood, Farqad A. Rashid, Zahraa Abbas, Areej A. Hateef, Haider s. Mohammed, Mohammed H. Ali, Sammah Dammaka, Radhia Dhahri, Ahmed RASHID, Tarek Saidani, "Optical behavior and its role in the antimicrobial properties of MgxCu1-xO nanoparticles", Journal of Positive Sciences, Vol. 4, Issue: 5, pp: 20-29, (2024). doi: https://doi.org/10.52688/ASP66329.
[58] Habiba K. Aity, Ruqaya Shaker Mahmood, Muwafaq A. Hasan, Mohammed RASHEED, Farqad A. Rashid, Zahraa Abbas, Areej A. Hateef, Haider s. Mohammed, Mohammed H. Ali, Sammah Dammaka, Radhia Dhahri, Ahmed RASHID, Nareman Chakchouk, "Exploring the structural features and antimicrobial functionality of Mg0.95Cu0.05O nanoparticles", Journal of Positive Sciences, Vol. 4, Issue: 5, pp: 30-40, (2024). doi: https://doi.org/10.52688/ASP57261.
[59] Habiba K. Aity, Rana A. Hadi, Ruqaya Shaker Mahmood, Mohammed RASHEED, Farqad A. Rashid, Zahraa Abbas, Areej A. Hateef, Ahmed RASHID, Nareman Chakchouk, "The relationship between optical characteristics and antibacterial

*Corresponding author
Mohammed RASHEED,
Applied Sciences Department, University of Technology, Baghdad, Iraq
e-mail: rasheed.mohammed40@yshoo.com

performance of Mg0.97Cu0.03O nanoparticles", Journal of Positive Sciences, Vol. 4, Issue: 5, pp: 30-40, (2024). doi: https://doi.org/10.52688/ASP33167.
[60] Habiba K. Aity, Kawther A. Alameri, Mohammed RASHEED, Ruqaya Shaker Mahmood, Farqad A. Rashid, Zahraa Abbas, Areej A. Hateef, Ahmed RASHID, Olfa Maalej, "The effect of structure on antibacterial performance of Mg0.94Cu0.06O nanoparticles", Journal of Positive Sciences, Vol. 4, Issue: 6, pp: 1-11, (2024). doi: https://doi.org/10.52688/ASP441661.
[61] Habiba K. Aity, Esra A. Hashem, Mohammed RASHEED, Ruqaya Shaker Mahmood, Farqad A. Rashid, Zahraa Abbas, Areej A. Hateef, Ahmed RASHID, Olfa Maalej, "The role of optical properties in enhancing antimicrobial activity of Mg0.94Cu0.06O nanoparticles", Journal of Positive Sciences, Vol. 4, Issue: 6, pp: 12-22, (2024). doi: https://doi.org/10.52688/ASP19241.
[62] Habiba K. Aity, Mohammed RASHEED, Kawther A. Alameri, Ruqaya Shaker Mahmood, Farqad A. Rashid, Zahraa Abbas, Areej A. Hateef, Ahmed RASHID, Marwa Enneffati, "Structural properties and bacterial inhibition capabilities of Mg0.91Cu0.09O nanoparticles", Journal of Positive Sciences, Vol. 4, Issue: 6, pp: 23-33, (2024). doi: https://doi.org/10.52688/ASP28610.
[63] Habiba K. Aity, Mohammed RASHEED, Esra A. Hashem, Ruqaya Shaker Mahmood, Farqad A. Rashid, Zahraa Abbas, Areej A. Hateef, Ahmed RASHID, Marwa Enneffati, "Assessing Optical Behavior and Antibacterial Potency of Mg0.91Cu0.09O Nanoparticles", Journal of Positive Sciences, Vol. 4, Issue: 6, pp: 34-43, (2024). doi: https://doi.org/10.52688/ASP80838.
[64] Mohammed RASHEED, Ketam K. Khudair, Habiba K. Aity, Ruqaya Shaker Mahmood, Farqad A. Rashid, Zahraa Abbas, Areej A. Hateef, Ahmed RASHID, Taha Rashid, "The impact of optical characteristics on antibacterial properties of Mg0.99Fe0.01O nanoparticles", Journal of Positive Sciences, Vol. 4, Issue: 6, pp: 54-63, (2024). doi: https://doi.org/10.52688/ASP75371.
[65] Mohammed RASHEED, Habiba K. Aity, Ketam K. Khudair, Ruqaya Shaker Mahmood, Farqad A. Rashid, Zahraa Abbas, Areej A. Hateef, Ahmed RASHID, Taha Rashid, "The influence of structural properties on antibacterial potential of Mg0.95Fe0.03O nanoparticles", Journal of Positive Sciences, Vol. 4, Issue: 6, pp: 64-74, (2024). doi: https://doi.org/10.52688/ASP50513.
[66] Ketam K. Khudair, Habiba K. Aity, Ruqaya Shaker Mahmood, Mohammed RASHEED, Farqad A. Rashid, Zahraa Abbas, Areej A. Hateef, Ahmed RASHID, Taha Rashid, "Optical analysis and its impact on antibacterial performance of Mg0.97Fe0.03O nanoparticles", Journal of Positive Sciences, Vol. 4, Issue: 6, pp: 75-86, (2024). doi: https://doi.org/10.52688/ASP88399.
[67] Rafal A. Obayed, Habiba K. Aity, Ruqaya Shaker Mahmood, Mohammed RASHEED, Farqad A. Rashid, Zahraa Abbas, Areej A. Hateef, Ahmed RASHID, Taha Rashid, "Investigating structural traits and their role in antibacterial properties of Mg0.94Fe0.06O nanoparticles", Journal of Positive Sciences, Vol. 4, Issue: 6, pp: 87-96, (2024). doi: https://doi.org/10.52688/ASP75220.

*Corresponding author
Mohammed RASHEED,
Applied Sciences Department, University of Technology, Baghdad, Iraq
e-mail: rasheed.mohammed40@yshoo.com